nature photonics

ARTICLES

PUBLISHED ONLINE: 9 NOVEMBER 2015 | DOI: 10.1038/NPHOTON.2015.216

X-ray imaging with scintillator-sensitized hybrid organic photodetectors

Patric Büchele[1,2]*, Moses Richter[3], Sandro F. Tedde[1], Gebhard J. Matt[3], Genesis N. Ankah[4], Rene Fischer[1,3], Markus Biele[1,3], Wilhelm Metzger[1], Samuele Lilliu[5], Oier Bikondoa[6,7], J. Emyr Macdonald[8], Christoph J. Brabec[3], Tobias Kraus[4], Uli Lemmer[2] and Oliver Schmidt[1]*

Medical X-ray imaging requires cost-effective and high-resolution flat-panel detectors for the energy range between 20 and 120 keV. Solution-processed photodetectors provide the opportunity to fabricate detectors with a large active area at low cost. Here, we present a disruptive approach that improves the resolution of such detectors by incorporating terbium-doped gadolinium oxysulfide scintillator particles into an organic photodetector matrix. The X-ray induced light emission from the scintillators is absorbed within hundreds of nanometres, which is negligible compared with the pixel size. Hence, optical crosstalk, a limiting factor in the resolution of scintillator-based X-ray detectors, is minimized. The concept is validated with a 256 × 256 pixel detector with a resolution of 4.75 lp mm^{-1} at a MTF = 0.2, significantly better than previous stacked scintillator-based flat-panel detectors. We achieved a resolution that proves the feasibility of solution-based detectors in medical applications. Time-resolved electrical characterization showed enhanced charge carrier mobility with increased scintillator filling, which is explained by morphological changes.

Today's most common flat-panel X-ray detectors for medical imaging consist of a scintillator that converts X-ray photons into light and a photodetector array made out of amorphous silicon[1,2]. The light emitted from the scintillator then propagates isotropically from the point of generation. This causes optical crosstalk between pixels, resulting in a low resolution. In addition to optical crosstalk, the detectors resolution is also limited by pixel size and electrical crosstalk due to trapped charges[3], for example. The resolution can be determined with the modulation transfer function (MTF), which describes the detectors' ability to transfer the input signal modulation of a given spatial frequency in relation to its output. An MTF value of 1 indicates the perfect detection of a given spatial frequency. To compare different detectors, it is practicable to determine the value of the spatial frequency f (measured in linepairs (lp) per mm) at which the MTF drops to 0.2. Advanced scintillators, such as thallium-doped cesium iodide (CsI:Tl), have a needle-type structure that behaves like a waveguide and decreases the optical crosstalk[4], resulting in f = 2–3 lp mm^{-1} at MTF = 0.2, depending on the thickness of the CsI:Tl[1]. However, CsI:Tl deposition is an expensive process and the material loses its crystal structure when exposed to humidity[5].

Direct-conversion detectors consist of a semiconductor material such as amorphous selenium (a-Se) that provides a high intrinsic X-ray absorption coefficient[6]. Because X-rays generate charges directly inside the semiconductor, these detectors have almost no optical crosstalk. While their resolution can be very high, it is limited by pixel size, electrical crosstalk and the operating electrical field. Current a-Se detectors have achieved f = 4.75 lp mm^{-1} at MTF = 0.2 (ref. 7). The field dependence of the ionization energy and the weak X-ray absorption necessitate thick layers, which result in very high operating voltages to achieve the electrical field required for an efficient charge extraction (~30 V μm^{-1}) (ref. 8).

Recently, several concepts have been proposed to leverage the advantages of organic semiconductors in medical flat-panel X-ray detectors requiring a size of up to 43 × 43 cm² (ref. 9). Organic photodiodes (OPDs) are attractive and cost-effective for this application as they can be processed from the solution phase over large, and even flexible, substrates[10,11]. OPD technology is based on an interpenetrating donor–acceptor network of an electron conductor, such as phenyl-C61-butyric acid methyl ester (PCBM), and a hole conductor, such as poly(3-hexylthiophene-2,5-diyl) (P3HT), which is known as a bulk heterojunction (BHJ)[12]. When a photon is absorbed by the BHJ, a Frenkel exciton is generated and can travel to the donor–acceptor interface, where it splits into an electron and a hole. The free charges can diffuse through the donor and acceptor percolation paths and reach their respective electrodes, thus enabling photodetection[13–15].

Appropriate nanoparticles can sensitize the absorption spectrum of pure P3HT:PCBM blends from the near-infrared to the X-ray region. Recently, OPDs have been enhanced with lead sulfide quantum dots for near-infrared detection[16]. Likewise, X-ray detection was demonstrated by adding small amounts of metal nanoparticles into a hole-conducting polymer[17].

Results and discussion

In this Article, we demonstrate that scintillating terbium-doped gadolinium oxysulfide (GOS:Tb) X-ray absorbers in the BHJ create a quasi-direct X-ray detector. The re-emitted photons from the scintillator particles are absorbed by the BHJ very close to the scintillator, minimizing optical crosstalk and enabling a high MTF. Low-cost micrometre-sized scintillator particles are used to achieve an optimum balance between high X-ray absorption and efficient charge extraction. The attenuation of GOS:Tb is above

[1]Siemens Healthcare GmbH, Technology Center, 91058 Erlangen, Germany. [2]Light Technology Institute and Institute of Microstructure Technology, Karlsruhe Institute of Technology, 76131 Karlsruhe, Germany. [3]Institute of Materials for Electronics and Energy Technology (i-MEET), Friedrich-Alexander-University Erlangen-Nuremberg, Martensstrasse 7, 91058 Erlangen, Germany. [4]INM – Leibniz Institute for New Materials, Campus D2 2, 66123 Saarbruecken, Germany. [5]Masdar Institute of Science and Technology, Abu Dhabi 54224, UAE. [6]XMaS, The UK-CRG Beamline, ESRF-The European Synchrotron, CS40220, Grenoble Cedex 9, 38043, France. [7]Department of Physics, University of Warwick, Gibbet Hill Road, Coventry CV4 7AL, UK. [8]School of Physics and Astronomy, Cardiff University, Queens Buildings, The Parade, Cardiff CF24 3AA, UK. *e-mail: patric.buechele@gmx.de; schmidt.oliver@siemens.com

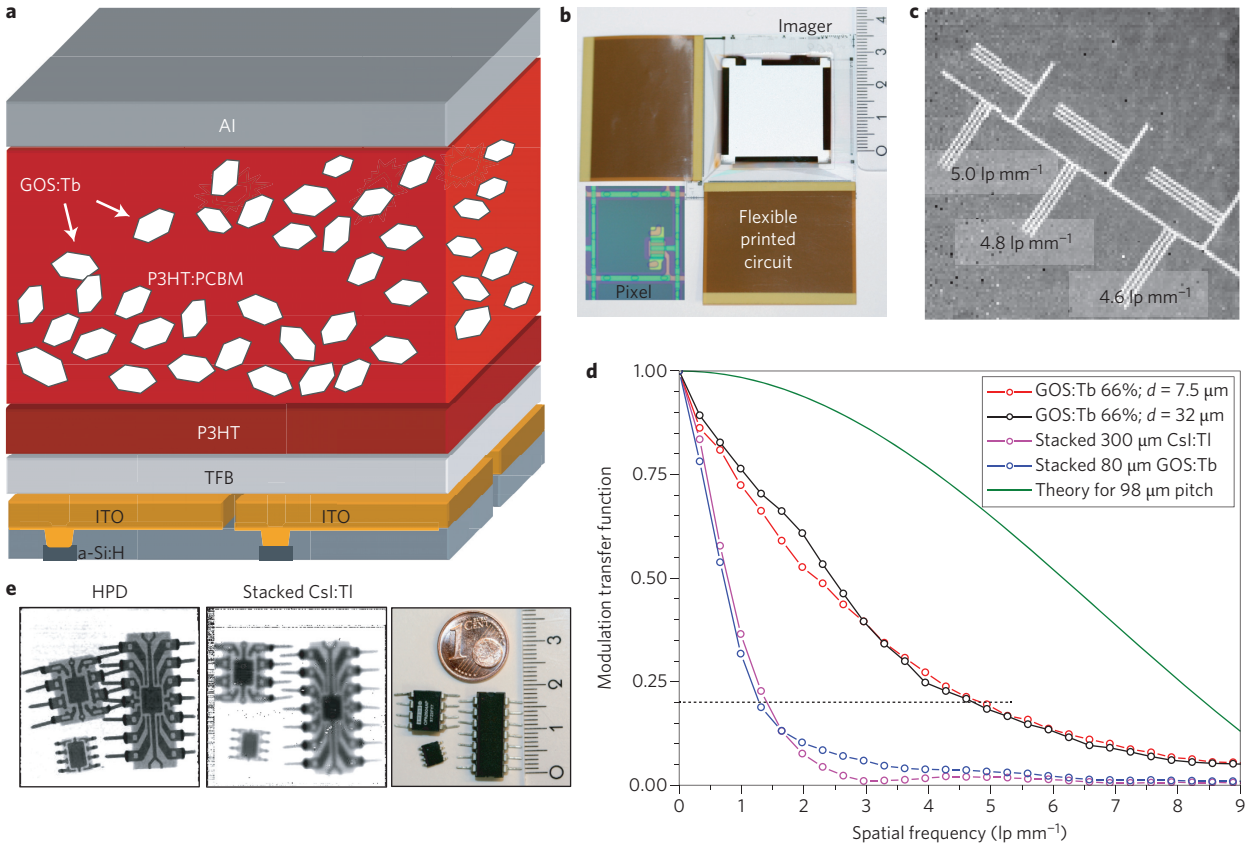

Figure 1 | Hybrid organic X-ray image sensor. a, Schematic of the image sensor with an a-Si:H backplane and a hybrid frontplane. **b**, Photograph of a fully processed imager and micrograph of an individual pixel with one TFT (98 µm pitch). **c**, 70 kV X-ray image (magnified to region of interest) of a resolution test target. **d**, MTF of HPD-imagers with different layer thickness (*d*) and two conventional indirect X-ray converters. The theoretical limit is determined by the pixel size. **e**, 70 kV X-ray images of integrated circuit devices (photograph on the right) realized with an HPD image sensor (left) and a conventional stacked device (centre).

that of CsI:Tl for X-rays <33 kV and >50 kV (ref. 1). The concept allows for adapting the scintillator/polymer material composition to the hardness of the radiation and is not limited to scintillators with anisotropic structures such as CsI:Tl.

We fabricated several X-ray image sensors with the structure depicted in Fig. 1a. The devices were based on an a-Si:H TFT array backplane with indium tin oxide (ITO) contact pads. Two interlayers of poly[(9,9-dioctylfluorenyl-2,7-diyl)-co-(4,4′-(N-(diphenylamine)]-butylphenyl)) (TFB) and P3HT were subsequently deposited on the backplane to reduce the dark current. Both interlayers form hole extracting/electron blocking contacts; in addition to the low intrinsic conductivity of TFB efficiently reducing electrical crosstalk (that is, between photodiodes). A suspension containing P3HT, PCBM and GOS:Tb was deposited on the interlayer by spray coating. The device stack was finalized by an electron selective aluminium (Al) top contact, deposited by thermal evaporation. The devices were encapsulated with epoxy glue and glass to avoid oxidation of the BHJ and Al electrode. Degeneration of the organic matrix on X-ray irradiation was observed, but the effect was small, reversible by thermal treatment, and should not represent a significant problem for medical X-ray imaging sensors[18]. A completed X-ray image sensor is shown in Fig. 1b.

The backplane matrix consists of 256 × 256 pixels with a pixel pitch of 98 µm, a geometric fill factor of ~70% and the pixel structure shown in the inset of Fig. 1b. A portion of the X-ray image of a resolution test target provided by using such a detector is shown in Fig. 1c. The image was recorded with an X-ray beam generated with 70 kV tungsten bremsstrahlung spectrum and filtered with 2.5 mm Al (dose rate 10 $mGy_{air}\,s^{-1}$, integration time ~22 ms, resulting in a dose of 220 μGy_{air}). The target area for the resolution tests consisted of line-pairs in a lead layer with a feature density between 4 and 5 lp mm^{-1}, all of which were resolved by the detector. The noise of our detectors was limited by a non-optimal read-out circuitry with a noise level of 8.000 electrons and the relatively high dark current of our detector. Further X-ray images and shelf-life measurements are reported in the Supplementary Information (see Supplementary Figs 1, 2).

The slanted-edge method measures the MTF to provide a quantitative resolution value[19]. Figure 1d demonstrates that for our hybrid photodetectors (HPDs), the resolution does not change with increasing thickness of the X-ray absorbing layer between 7.5 µm to 32 µm. Preliminary results (data not shown) with a 170 µm thick layer showed similar resolution. The spatial frequency at which the MTF drops to 0.2 was 4.75 lp mm^{-1}, which is comparable to a state-of-the-art a-Se detector[7]. The resolution of our demonstrator device lies below the theoretical limit, probably due to the pixel-to-pixel and trap-assisted electrical crosstalk that are known from direct converters. Our hybrid detector clearly outperforms indirect converters with a stacked scintillator (80 µm GOS:Tb and 300 µm CsI:Tl) mounted on top of an OPD, as is clear in the side-by-side comparison of X-ray images of integrated circuits in Fig. 1e.

Here we use test diode structures to study the fundamental physical properties and limitations of HPDs. The scanning electron microscopy (SEM) images in Fig. 2a–c show cross-sections of HPDs prepared with focused ion beam (FIB) with three different volume ratios of GOS:Tb: 40 vol% (the weight ratio of P3HT:PCBM:GOS:Tb was 1:1:8), 66 vol% (1:1:24) and 80 vol% (1:1:48). Isolated GOS:Tb particles (bright) are surrounded by a

homogeneous P3HT:PCBM BHJ (dark). The GOS:Tb particles were fully embedded in the organic matrix for samples with 40 vol%, while voids (marked with red boxes) occurred increasingly at higher fractions of GOS:Tb due to the limited amount of organic material. X-ray absorption increased with GOS:Tb content up to a 66 vol%. At higher GOS:Tb fractions the packing density of the solid particles limited their final volume fraction, causing the formation of voids (see Supplementary Fig. 3), and saturating X-ray absorption.

From an optical perspective, the optimum volume ratio between particles and BHJ depends on the emission properties of the particle and the absorption properties of the BHJ. The dominating green emission of X-ray excited GOS:Tb has a large overlap with the absorption spectra of P3HT:PCBM (see Supplementary Fig. 4), which results in a small penetration depth (130 nm). A core–shell model that assumes an average size for the GOS:Tb particles (1.8 μm diameter) predicts an ideal volume ratio between X-ray converting GOS:Tb cores and photon-absorbing BHJ shells of 67 vol%. Particle contents below this 'golden filling factor' limit X-ray absorption and the generation of charge carriers, while particle concentrations above perturb the extraction of photogenerated charge carriers. The 3D profiles also show that the detector surfaces become rougher with increasing GOS:Tb fractions (Fig. 2d–f). Excess GOS:Tb at the top surface aggregates during the spray coating process and inhibits the formation of a good metal contact. The resulting defects at this interface play an important role in the following discussion.

We studied the effect of the filling factor on the electrical properties and the X-ray response. The amount of GOS:Tb in the dispersion was gradually increased from a weight ratio between P3HT:PCBM:GOS:Tb of 1:1:0 (0 vol%) up to 1:1:48 (80 vol%). Test devices with the same layer stack as described above and a diode area of 1 cm^2 were processed and characterized electrically in the dark and under X-ray irradiation. The dark current density in reverse bias of HPDs is an important measure for the minimal detectable signal and should be as low as possible. Figure 3a shows virtually identical dark current densities under reverse bias for all devices except for the 80 vol% device, which was probably dominated by defects at the interface with the top contact (Fig. 2c,f). The injected current density at forward bias (the Al contact was negative in respect to the ITO) increases with a higher GOS:Tb filling fraction. This is unexpected—the addition of insulators to the device should not improve charge carrier transport. The pure 0 vol% P3HT:PCBM device showed the highest rectification. As outlined later in greater detail, the morphology and consequently the nature of the charge transport of the BHJ changes dramatically with the addition of the GOS:Tb particles.

An important sensitivity measure of an HPD is the response to X-ray radiation. Figure 3b shows the X-ray sensitivity S of our samples:

$$S = \frac{Q}{eDA} = \frac{\int (I_{\text{X-ray}}(t) - I_{\text{dark}})\mathrm{d}t}{eDA} \quad (1)$$

where $I_{\text{X-ray}}$ and I_{dark} represent the current under X-ray irradiation and in the dark, respectively, e represents the elementary charge, D the X-ray entrance dose in air, which is commonly used in medical applications to calculate the patient or organ dose[20] (defined in detail in the Supplementary Information), and A, the active area of the HPD. The equation expresses the number of extracted charge carriers Q/e generated by X-ray radiation per D and per A. At low filling ratios, S increased with the fraction of GOS:Tb due to increasing X-ray absorption. At a bias of 0 V, S had a maximum at a GOS:Tb fraction of around 60 vol%, close to the golden filling factor discussed above. It decreased at higher GOS:Tb loading due to degrading charge transport in the remaining BHJ.

An external bias of −10 V increased S in detectors with little GOS:Tb by almost one order of magnitude because the bias improved charge carrier extraction. In detectors with GOS:Tb contents above the golden filling factor, S increased dramatically when an external field was applied. This may be explained by a photoconductive gain mechanism, as reported before[21]. The electric field density was more concentrated in the organic phase and the increasing roughness with higher GOS:Tb fraction additionally increases field emission at the Al contact[22,23]. Morphological changes (described below) at high filling ratios are likely to cause an unbalanced transport behavior. We observed slow reaction times (see Supplementary Fig. 7) and a photoconductor-type response (see Supplementary Fig. 8) at high GOS:Tb contents.

An X-ray sensitivity of $S = 360\ e^-\ nGy^{-1}\ mm^{-2}$ for the 50 vol% HPD device at $-10\ V\ \mu m^{-1}$ corresponds to an electron–hole pair generation energy of 68 eV (see Supplementary Information for details), which is slightly larger than an a-Se direct converter at an electrical field of $10\ V\ \mu m^{-1}$ (ref. 6).

The pulse response time is an important factor when imaging dynamic objects with short X-ray pulses. The transient current response of the 57 vol% device on X-ray irradiation is plotted in Fig. 3c. X-ray pulses with a dose rate of $1.5\ mGy_{air}\ s^{-1}$ and a pulse duration of 100 ms were applied and the bias was varied between 0 V and −10 V ($0\ V\ \mu m^{-1}$ and $-1\ V\ \mu m^{-1}$). The dark current was subtracted for better comparison. Figure 3d shows that the rise time (from 10 to 90% of the maximum signal) and the fall time (from 90 to 10%) decreased for higher bias. There was no saturation of the current response within the pulse length of 100 ms for any bias: Arguably trap states at the metal/semiconductor interface are responsible for the slow response[24,25].

The remaining technological challenges are the relatively high dark current density and the slow response time. Both depend crucially on oxygen doping induced during spray coating in ambient conditions and interface traps between the electrodes and semiconductor[26]. Both will be addressed by work function and interlayer tuning as well as by oxygen-free deposition methods[27].

A new method was required to analyse the charge transport mechanism of the thick HPDs. For this purpose, we developed X-ray excited charge carrier extraction by linearly increasing voltage (X-CELIV) to probe the mobility of X-ray-generated charges by measuring the transient current during a voltage ramp. In X-CELIV, charge carriers are excited throughout the bulk layer, which provides the possibility of studying an HPD in a similar manner to photo-CELIV[28]. In X-CELIV the mobility of the X-ray generated free charge carriers are measured by analysing the temporal charge extraction on depletion of the sample. Charge carrier depletion is achieved by applying a voltage ramp (for example, from 0 to 20 V). The elegance of the CELIV method lies in the fact that the sample is analysed under the actual working conditions and no further sample preparations/modifications are necessary. The inset in Figure 4a shows a representative X-CELIV signal in dark (black line) and after an X-ray pulse (red line). The X-CELIV signal can be divided into two main features, a relatively rapidly increasing signal followed by a slower decay, and second signal of a constant positive offset (boxcar function). This offset describes the displacement current of the sample capacitance, whereas the extracted charge carriers from the sample cause the first extraction peak. After X-ray exposure, an enhanced extraction peak due to the increased free charge carrier concentration is observed, and the maximum is shifted to a shorter time scale.

The effective drift mobility of the exited free charges in the P3HT:PCBM is calculated from the time delay of the peak maximum relative to the onset of the rectangular signal[29–31]. Figure 4a shows the charge carrier mobility as function of the GOS:Tb volume fraction. The mobility increased by two orders of magnitude when varying GOS:Tb fractions between 25 and 80 vol% and was comparable to current literature[28,32]. We attribute this increase to an increasingly crystalline organic blend at higher

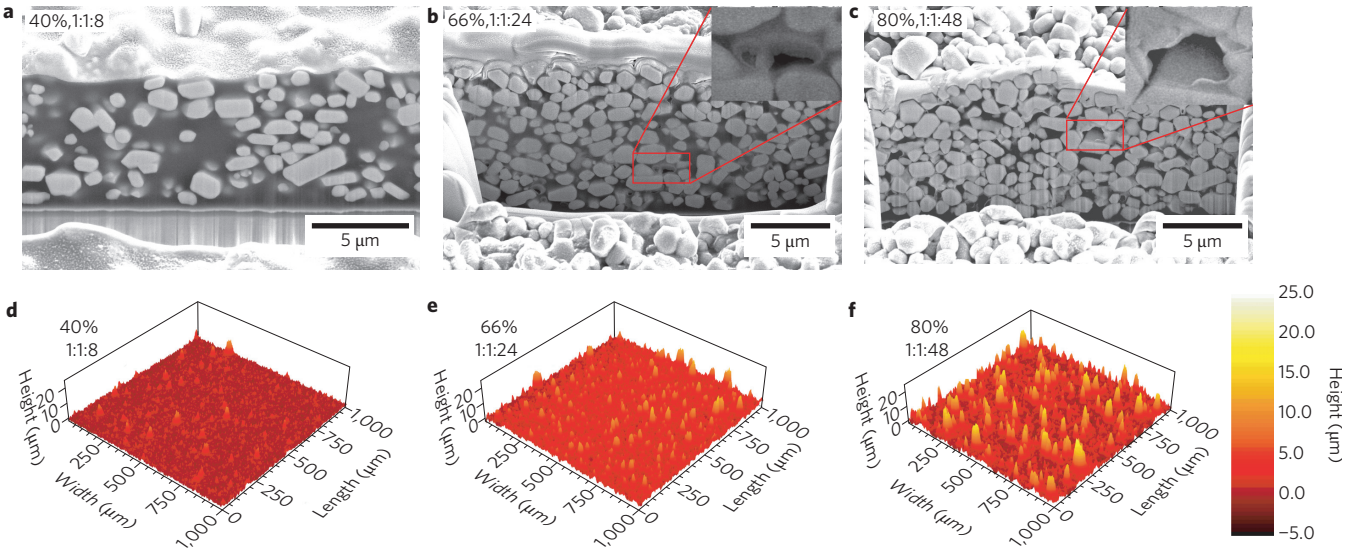

Figure 2 | Influence of scintillator fraction on layer morphology. a–c, SEM cross-sections (FIB cuts with 52° tilt angle), red boxes and insets highlight voids inside the devices. **d–f**, 3D surface profilometry of samples. Scanning resolution is 1 µm in both axis.

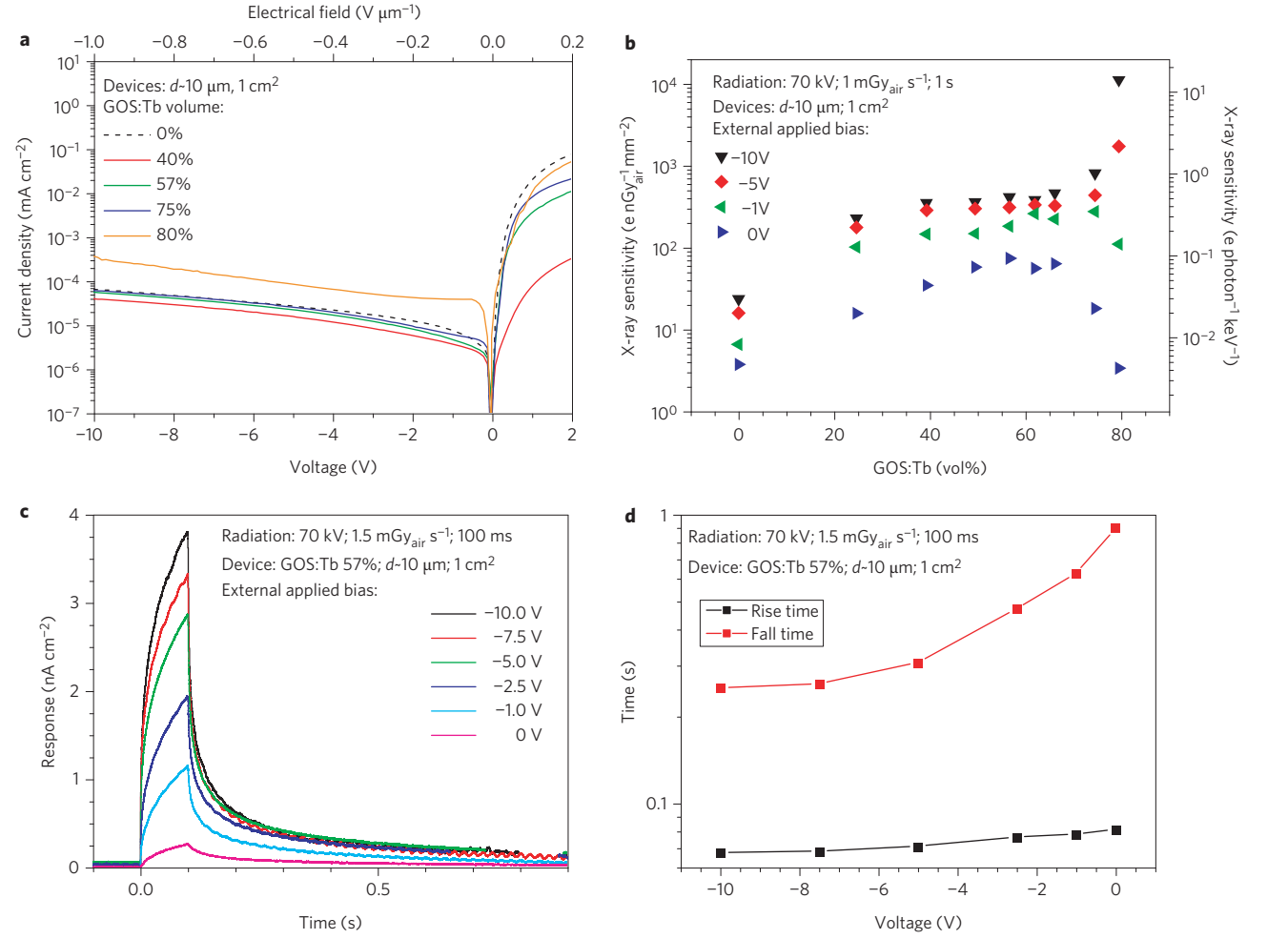

Figure 3 | Optoelectronical properties of HPDs. a, Dark current–voltage characteristics with different GOS:Tb volume fractions and an active area of 1 cm². **b**, X-ray sensitivity irradiated with a spectrum of 70 kV bremsstrahlung and dose rate of 1 mGy_{air} s^{-1} at different external bias. **c**, Pulse response of the 57 vol%-HPD biased from 0 to –10 V (0 to –1 V µm^{-1}); dose rate: 1.5 mGy_{air} s^{-1}, 100 ms pulse duration. **d**, Corresponding rise (black) and fall (red) time dependent on the applied bias.

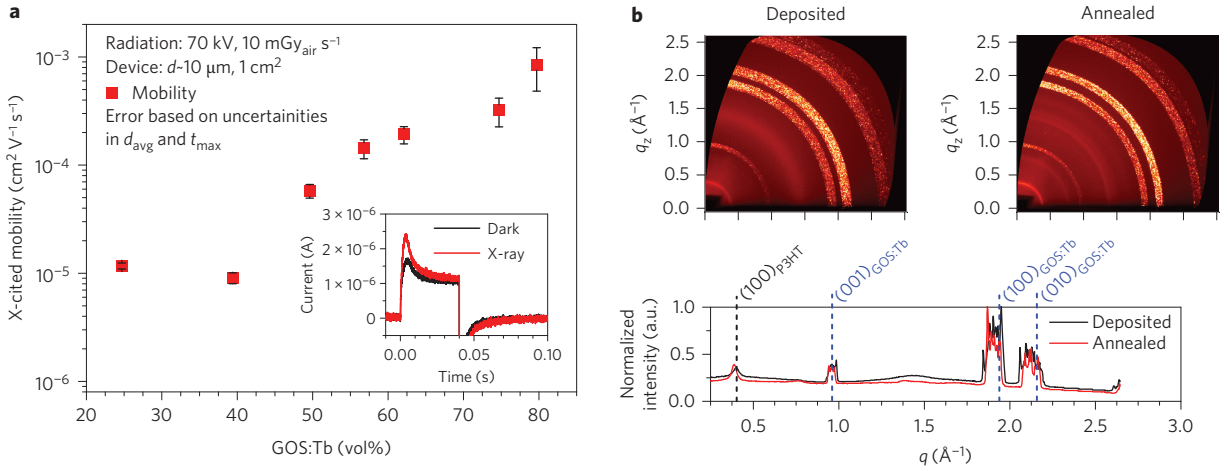

Figure 4 | Mobility and morphology characteristics. a, X-CELIV properties with different GOS:Tb volume fraction. The inset represents a typical X-CELIV peak. The error bars are based on the uncertainties in the average layer thickness d_{avg} and reading the time of the current maximum t_{max}. **b**, GIWAXS Debye–Scherrer rings and out-of-plane line profiles, incident angle $a_i = 0.24°$, $\chi = 15°$ while the x-axis represents q_{xy}, the 57% (1:1:16) HPD as deposited and annealed. Intensity has been normalized, while the x-axis represents the absolute value of the scattering vector q.

GOS:Tb fractions. This would also explain the decreasing series resistance of the devices that occurred at high GOS:Tb filling. The mobility values imply charge carrier drift lengths around 74 µm.

Synchrotron grazing-incidence wide-angle X-ray scattering (GIWAXS) annealing studies have been performed to investigate the changes in polymer microstructure induced by GOS:Tb[33–36]. Figure 4b shows the diffraction patterns of a 5 µm-thick film at a volume ratio of 57 vol% before and after annealing for 10 min at 150 °C and the corresponding out-of-plane line profiles (other filling fractions are shown in Supplementary Table 10). GOS:Tb peak clusters have been indexed according to refs 37–39. Annealing caused an increase in the domain size of P3HT along the *a* crystal direction (the (100) peak narrows) and a permanent expansion of the *a* lattice constant (the (100) peak position moves to lower scattering vector q values)[35,40]. We also determined a structural interplay between P3HT and GOS:Tb during drying and annealing of the film. The amount of P3HT face-on lamella increased with GOS:Tb concentration (see Supplementary Fig. S13). Lamellar parts exhibit improved hole conduction (π-hopping) within the P3HT crystalline domains, and therefore an increase mobility of the X-ray induced charges[35,41]. An explanation may be that the GOS:Tb acts as a crystallization seed for P3HT, a finding supported by the recent observation of changing morphology on the incorporation of inorganic particles in a BHJ[42].

Conclusion

In this work we have presented a novel approach to fabricating new X-ray imaging devices, involving quasi-direct conversion by incorporation of micrometre-scale GOS:Tb scintillator particles directly into an organic semiconductor photoactive layer. X-ray images of the hybrid sensors resolved fine features without optical crosstalk. This was expressed by an excellent spatial resolution of 4.75 lp mm^{-1} at MTF = 0.2, which is on par with recent commercial a-Se direct converters. A detailed analysis of the HPD devices reveals an X-ray sensitivity of 459 e$^-$ nGy$_{air}^{-1}$ mm^{-2} at collection field of −1 V µm^{-1} at volume fractions of the golden filling factor of 67%. At volume fractions above the golden filling factor we observed photoconductive gain at −1 V µm^{-1}. GIWAXS and X-CELIV studies clearly correlated the morphology and charge carrier mobility of thick hybrid devices. Surprisingly, the charge carrier mobility increased with higher volume fractions of GOS:Tb, allowing efficient charge extraction from layer thicknesses of 10 µm and above. Spray coating of thick layers promises to be a low-cost and high-throughput production method for devices with large active areas. This technology can potentially achieve benchmark results compared to today's state-of-the-art direct converters fabricated from a-Se, with the additional benefits of a drastically relaxed demand on external bias, potentially much lower production costs and a higher absorption coefficient for high-energy X-ray photons >50 keV.

Methods

Methods and any associated references are available in the online version of the paper.

Received 16 March 2015; accepted 5 October 2015; published online 9 November 2015; corrected online 13 November 2015

References

1. Spahn, M. Flat detectors and their clinical applications. *Eur. Radiol.* **15,** 1934–1947 (2005).
2. Pacella, D. Energy-resolved X-ray detectors: the future of diagnostic imaging. *Rep.Med. Imag.* **8,** 1–13 (2015).
3. Kabir, M. Z. *et al.* Direct conversion x-ray sensors: Sensitivity, DQE and MTF. *IEEE Proc. Circ. Dev. Syst.* **150,** 258–266 (2003).
4. Zhao, W., Ristic, G. & Rowlands, J. A. X-ray imaging performance of structured cesium iodide scintillators. *Med. Phys.* **31,** 2594–2605 (2004).
5. Pin, Y., Harmon, C. D., Doty, F. P. & Ohlhausen, J. A. Effect of humidity on scintillation performance in Na and Tl activated CsI crystals. *IEEE Trans. Nucl. Sci.* **61,** 1024–1031 (2014).
6. Kasap, S. *et al.* Amorphous and polycrystalline photoconductors for direct conversion flat panel x-ray image sensors. *Sensors* **11,** 5112–5157 (2011).
7. Kabir, M. Z. *et al.* Effect of repeated x-ray exposure on the resolution of amorphous selenium based x-ray imagers. *Med. Phys.* **37,** 1339–1349 (2010).
8. Kasap, S. O. X-ray sensitivity of photoconductors: application to stabilized a-Se. *J. Phys. D* **33,** 2853–2865 (2000).
9. Gelinck, G. H. *et al.* X-ray imager using solution processed organic transistor arrays and bulk heterojunction photodiodes on thin, flexible plastic substrate. *Org. Electron.* **14,** 2602–2609 (2013).
10. Tedde, S. F. *et al.* Fully spray coated organic photodiodes. *Nano Lett.* **9,** 980–983 (2009).
11. Krebs, F. C. *et al.* A round robin study of flexible large-area roll-to-roll processed polymer solar cell modules. *Sol. Energy Mater. Sol. Cells* **93,** 1968–1977 (2009).
12. Brabec, C. J. *et al.* Polymer–fullerene bulk-heterojunction solar cells. *Adv. Mater.* **22,** 3839–3856 (2009).
13. Kraabel, B. *et al.* Ultrafast photoinduced electron transfer in conducting polymer buckminsterfullerene composites. *Chem. Phys. Lett.* **213,** 389–394 (1993).
14. Heeger, A. J. 25th anniversary article: bulk heterojunction solar cells: understanding the mechanism of operation. *Adv. Mater.* **26,** 10–28 (2014).
15. Brabec, C. J., Sariciftci, N. S. & Hummelen, J. C. Plastic solar cells. *Adv. Funct. Mater.* **11,** 15–26 (2001).

16. Rauch, T. *et al.* Near-infrared imaging with quantum-dot-sensitized organic photodiodes. *Nature Photon.* **3,** 332–336 (2009).
17. Mills, C. A. *et al.* Enhanced x-ray detection sensitivity in semiconducting polymer diodes containing metallic nanoparticles. *J. Phys. D* **46,** 275102 (2013).
18. Street, R. A., Northrup, J. E. & Krusor, B. S. Radiation induced recombination centers in organic solar cells. *Phys. Rev. B* **85,** 205211 (2012).
19. Samei, E., Flynn, M. J. & Reimann, D. A. A method for measuring the presampled MTF of digital radiographic systems using an edge test device. *Med. Phys.* **25,** 102–113 (1998).
20. International Commission on Radiation Units. Patient dosimetry for X rays used in medical imaging. *J. ICRU* **5,** http://dx.doi.org/10.1093/jicru/ndi016 (2005).
21. Chen, H.-Y., LoMichael, K. F., Yang, G., Monbouquette, H. G. & Yang, Y. Nanoparticle-assisted high photoconductive gain in composites of polymer and fullerene. *Nature Nanotech.* **3,** 543–547 (2008).
22. Fowler, R. H. & Nordheim, L. *Electron Emission in Intense Electric Fields* (Royal Society, 1928).
23. Heeger, A. J., Parker, I. D. & Yang, Y. Carrier injection into semiconducting polymers: Fowler-Nordheim field-emission tunneling. *Synthetic Met.* **67,** 23–29 (1994).
24. Oehzelt, M., Koch, N. & Heimel, G. Organic semiconductor density of states controls the energy level alignment at electrode interfaces. *Nature Commun.* **5,** 4174 (2014).
25. Vázquez, H. *et al.* Barrier formation at metal organic interfaces: dipole formation and the charge neutrality level. *Appl. Surf. Sci.* **234,** 107–112 (2004).
26. Büchele, P. *et al.* Space charge region effects in bidirectional illuminated P3HT: PCBM bulk heterojunction photodetectors. *Org. Electron.* **22,** 29–34 (2015).
27. Saracco, E. *et al.* Work function tuning for high-performance solution-processed organic photodetectors with inverted structure. *Adv. Mater.* **25,** 6534–6538 (2013).
28. Mozer, A. J. *et al.* Charge transport and recombination in bulk heterojunction solar cells studied by the photoinduced charge extraction in linearly increasing voltage technique. *Appl. Phys. Lett.* **86,** 112104 (2005).
29. Juška, G. *et al.* Extraction current transients: new method of study of charge transport in microcrystalline silicon. *Phys. Rev. Lett.* **84,** 4946 (2000).
30. Juška, G. *et al.* Extraction of photogenerated charge carriers by linearly increasing voltage in the case of Langevin recombination. *Phys. Rev. B* **84,** 155202 (2011).
31. Nekrašas, N. *et al.* Features of current transients of photogenerated charge carriers, extracted by linearly increased voltage. *Chem. Phys.* **404,** 56–59. (2012).
32. Garcia-Belmonte, G. *et al.* Charge carrier mobility and lifetime of organic bulk heterojunctions analyzed by impedance spectroscopy. *Org. Electron.* **9,** 847–851 (2008).
33. Lilliu, S., Alsari, M., Bikondoa, O., Macdonald, J. E. & Dahlem, M. S. Absence of structural impact of noble nanoparticles on P3HT: PCBM blends for plasmon enhanced bulk-heterojunction organic solar cells probed by synchrotron GI-XRD. *Sci. Rep.* **5,** 10633 (2015).
34. Lilliu, S. *et al.* The influence of substrate and top electrode on the crystallization dynamics of P3HT:PCBM blends. *Energy Proc.* **31,** 60–68 (2012).
35. Lilliu, S. *et al.* Dynamics of crystallization and disorder during annealing of P3HT/PCBM bulk heterojunctions. *Macromolecules* **44,** 2725–2734 (2011).
36. Lilliu, S. *et al.* Effects of thermal annealing upon the nanomorphology of poly (3-hexylselenophene)-PCBM blends. *Macromol. Rapid Comm.* **32,** 1454–1460 (2011).
37. Huang, J. *et al.* Gd2O2S:Eu3+ and Gd2O2S:Eu3+/Gd2O2S hollow microspheres: Solvothermal preparation and luminescence properties. *J.Alloy. Compd.* **532,** 34–40 (2012).
38. Onoda, M., Chen, X.-a., Sato, A. & Wada, H. Crystal structure of Cu2Gd2/3S2: interlayer short-range order of Gd vacancies. *J. Solid State Chem.* **152,** 332–339 (2000).
39. Eick, H. A. The preparation, lattice parameters and some chemical properties of the rare earth mono-thio oxides. *J. Am. Chem. Soc.* **80,** 43–44 (1958).
40. Verploegen, E. *et al.* Effects of thermal annealing upon the morphology of polymer–fullerene blends. *Adv. Funct. Mater.* **20,** 3519–3529 (2010).
41. Pingree, L. S. C., Reid, O. G. & Ginger, D. S. Imaging the evolution of nanoscale photocurrent collection and transport networks during annealing of polythiophene/fullerene solar cells. *Nano Lett.* **9,** 2946–2952 (2009).
42. González, D. M. *et al.* Improved power conversion efficiency of P3HT: PCBM organic solar cells by strong spin–orbit coupling-induced delayed fluorescence. *Adv. Eng. Mater.* http://dx.doi.org/10.1002/aenm.201401770 (2015).

Acknowledgements

We thank the German Federal Ministry for Education and Research (BMBF) for funding this work (13N12377). P.B. is recipient of an Ernst von Siemens Doctoral Fellowship (Ernst-von-Siemens-Promotionsstipendium). Siemens Healthcare GmbH group thanks S. Szyszkowski and J. Hürdler for their enduring support. C.J.B. acknowledges funding by the Bavarian Ministry of Economic Affairs and Media, Energy and Technology for the Joint Projects of the Helmholtz-Institute Erlangen-Nürnberg for Renewable Energy Production (HI ERN). M.R. thanks the German Research Foundation (DFG) for financial support through the Graduate School GRK 1896. We thank B. Curzadd for contributing with the design of a new GIWAXS chamber and for fabricating the chamber itself. We thank the XMaS beamline team for the support at the beamline, and M. S. Dahlem and M. Alsari for the help with the measurements at the beamline. G.N.A. and T.K. thank E. Arzt for his continuing support of the project.

Author contributions

P.B. carried out device fabrication and characterization, and analysis of the results. M.R. executed X-CELIV experiments. G.N.A. executed FIB-cutting and SEM experiments. S.F.T. executed X-ray imaging and XRD measurements, as well as X-ray device analysis. R.F. executed X-ray imaging and arranged X-ray setup. M.B. executed and helped with analysis of pulse measurements. W.M. executed GOS:Tb characterization. G.J.M. conducted and helped with the X-CELIV measurement. S.L. directed, executed and analysed XRD experiments. O.B. set up the synchrotron beamline. J.E.M. submitted the proposal for XRD experiments and helped with the XRD analysis. C.J.B. directed and helped with X-CELIV analysis. T.K. directed and helped with FIB/SEM analysis. U.L. helped with optoelectronical characterization and analysis of X-ray response measurements. O.S. directed device fabrication, and helped with device analysis.

Additional information

Supplementary information is available in the online version of the paper. Reprints and permissions information is available online at www.nature.com/reprints. Correspondence and requests for materials should be addressed to P.B. and O.S.

Competing financial interests

The authors declare no competing financial interests.

Methods

Device manufacturing. The device architecture for the reference diodes and imagers is a structured ITO substrate with a TFB (80 nm) interlayer. An additional pure P3HT interlayer (500 nm) overlies this, followed by hybrid BHJ containing P3HT:PCBM:GOS:Tb with a weight ratio of 1:1:x (x = 0–48), finished by an aluminium top contact. The reference diode area was 1 cm² defined by the size of the openings in the passivation layer (SU-8 Photoresist) on top of the ITO contact. After cleaning with *N*-Methyl-2-pyrrolidon and Mucasol in an ultrasonic bath the ITO was activated by RIE oxygen plasma for 10 min. The TFB interlayer was deposited by spin coating and annealed for 2 h at 200 °C in a vacuum oven (10^{-2} mbar), whereas the P3HT and hybrid BHJ were deposited by spray coating[2]. The P3HT solution and the hybrid suspension containing P3HT, PCBM and GOS:Tb with a ratio of 1:1:x and total mass content of 2% were stirred for three days (inert atmosphere, at room temperature) and filtered (0.1 μm and 5 μm PTFE, respectively) before spray coating. The samples were annealed on a hotplate after deposition (nitrogen glove box conditions, 140 °C, 10 min), followed by evacuation process for 24 h in an evaporator (10^{-6} mbar). A 0.3 μm-thick aluminium top contact was evaporated at an average deposition rate of 0.2 nm s^{-1}. After evaporation, an additional annealing step was performed (140 °C; 10 min). Reference X-ray detectors were established by processing a 650 nm layer of P3HT:PCBM on the TFT panels and evaporating a semitransparent calcium:silver (Ca:Ag) top contact. All devices were protected with a 100 μm quartz glass against oxygen and moisture. A commercial-grade 300 μm CsI:Tl scintillator screen was then glued with epoxy onto the image detector to record X-ray images.

Image read-out and processing. Images from the 256 × 256 TFT panel were read by a read-out IC (ROIC). The signal at the input was simultaneously integrated, amplified, low pass filtered and converted from analog to digital with a 14-bit converter. The integrator feedback capacitance C_f was 1 pF, the integration time 20 ms. Noise produced by the external readout electronics TFT detector panel was characterized by taking dark images without and with sensor. To eliminate fixed pattern noise, two different dark images were subtracted. The mean value and the standard deviation were deduced from a region of interest (ROI). The standard deviation presents the electronic noise in numbers of electrons. The noise of the electronic read out circuit was 8.000 electrons. X-ray recordings from objects were offset compensated by subtracting a dark image and flat-field corrected by calculating the gain factor of each pixel from a flat-field image.

The modulation transfer function (MTF) is determined by the slanted-edge method. First an object with a sharp edge is placed on the X-ray detector and the edge profile is derived from the resulting X-ray image. The line spread function (LSF) is derived by differentiating the edge profile. The Fourier transform of the LSF defines the MTF.

Optoelectronic device and material characterization. Absorption data of the BHJ were measured with a Perkin Elmer Spectrometer UV–VIS Lambda 2, IV/JE characteristics were measured by a Keithley 6,487 picoamperemeter, X-ray dose rates were measured with a PTW Diados dosemeter, and profile data were measured with a KLA Tencor PT15. X-ray radiation was generated by a rotating anode X-ray tube. The spectrum of the bremsstrahlung corresponds to a tungsten anode and was filtered by 2.5 mm Al. The stated dose is the entrance dose in air (D), measured in air at the surface of the sample. An acceleration voltage of 70 kV between glowing cathode and tungsten anode was used to generate the X-ray photons. The air KERMA or D is commonly used in medical applications to give a measurement parameter for the dose a patient is exposed to. This parameter is used to calculate the patient or organ dose. Therefore D in mGy_{air} allows a comparison with any other medical detector. A detailed description of the dose calculations in medical imaging is presented in the report of the International Commission on Radiation Units (ICRU)[20]. Alternatively, the units of the X-ray sensitivity S given in (e^- nGy_{air}^{-1} mm^{-2}) can be also expressed in (e^- $photons^{-1}$ keV^{-1}). This can be done by substituting the 1 nGy_{air} with 803 photons keV mm^{-2} (see Supplementary Information for details).

The emission spectrum of GOS:Tb was measured with a Varian Cary Eclipse spectrometer. A thin powder layer (0.5 mm) was enclosed in a highly reflecting Teflon holder and excited by a narrowband 227 nm UV source. The emitted light was spectrally filtered and detected by a photomultiplier tube using an emission slit of 2.5 nm.

Structural characterization via focused ion beam preparation and scanning electron microscopy. Composites of P3HT:PCBM:GOS:Tb were coated with 10–20 nm thick Au layers to improve the sample conductivity during electron microscopy. The active layers of the devices consisting of composites of conductive polymers and functional inorganic particles were studied using an FEI Versa 3D DualBeam FIB microscope. We used an FIB to mill into the bulk of a specimen and analysed its internal microstructure. The FIB was equipped with a Gallium ion source and operated at 30 kV in a current range of 50 pA to 1 nA. A FIB cuts through the soft polymer matrix that intersects the hard GOS:Tb particles and can cause artifacts in the microstructure such as ridges and grooves. In addition, the high-energy ion bombardment may lead to the local creation of amorphous layers. Beam damage was minimized and a smooth cross-section was achieved using low milling currents of 50–100 pA in a final 'cleaning' step. FIB cuts were prepared at several positions on the devices to obtain an overview of the microstructure of the hybrid diode layer. Scanning electron microscopy (SEM) imaging (the beam was arranged at a 52° tilt angle) was then performed on the cross-section to study the distribution of the particles and the occurrences of voids in the composites. The microstructures were analysed using the secondary electron detector.